



Cite this: *Nanoscale*, 2015, 7, 18138

## Seamless lamination of a concave–convex architecture with single-layer graphene†

Ji-Hoon Park,<sup>‡a</sup> Taekyung Lim,<sup>‡b</sup> Jaeyoon Baik,<sup>c</sup> Keumyoung Seo,<sup>b</sup> Youngkwon Moon,<sup>a</sup> Noejung Park,<sup>d</sup> Hyun-Joon Shin,<sup>c</sup> Sang Kyu Kwak,<sup>\*e</sup> Sanghyun Ju<sup>\*b</sup> and Joung Real Ahn<sup>\*a</sup>

Graphene has been used as an electrode and channel material in electronic devices because of its superior physical properties. Recently, electronic devices have changed from a planar to a complicated three-dimensional (3D) geometry to overcome the limitations of planar devices. The evolution of electronic devices requires that graphene be adaptable to a 3D substrate. Here, we demonstrate that chemical-vapor-deposited single-layer graphene can be transferred onto a silicon dioxide substrate with a 3D geometry, such as a concave–convex architecture. A variety of silicon dioxide concave–convex architectures were uniformly and seamlessly laminated with graphene using a thermal treatment. The planar graphene was stretched to cover the concave–convex architecture, and the resulting strain on the curved graphene was spatially resolved by confocal Raman spectroscopy; molecular dynamic simulations were also conducted and supported the observations. Changes in electrical resistivity caused by the spatially varying strain induced as the graphene–silicon dioxide laminate varies dimensionally from 2D to 3D were measured by using a four-point probe. The resistivity measurements suggest that the electrical resistivity can be systematically controlled by the 3D geometry of the graphene–silicon dioxide laminate. This 3D graphene–insulator laminate will broaden the range of graphene applications beyond planar structures to 3D materials.

Received 17th June 2015,  
Accepted 27th September 2015

DOI: 10.1039/c5nr04004c

www.rsc.org/nanoscale

## Introduction

Graphene, with its excellent physical properties, has replaced the essential parts of various electronic, optical, and mechanical devices, which has resulted in innovative enhancements in the performance of these devices.<sup>1–4</sup> Various forms of graphene, such as mechanically exfoliated graphene, graphene

oxides, epitaxial graphene, and graphene grown by chemical vapor deposition (CVD), have been developed and used for different purposes in research and for various applications.<sup>1,5–7</sup> In particular, CVD graphene has been widely used in applications because of the advantages of wafer-scale growth, transferability to a specific substrate, and sufficient mobility and conductance. CVD graphene has contributed to the development of high-frequency transistors, solar cells, light-emitting diodes, touch screens, photodetectors, nonvolatile memory, and thermoelectric devices.<sup>8–14</sup> Recently, the quality of CVD graphene has advanced to enable new functions in devices: lateral and vertical heterogeneous junctions of layered materials,<sup>15,16</sup> foam architecture,<sup>17</sup> and 3D designed graphene.<sup>18</sup>

Another dimension in the evolution of the application of CVD graphene to devices is related to the recent development of two representative real devices: memory and displays.<sup>19,20</sup> These real devices exhibit a complicated, multiple-stacked geometry with a concave–convex architecture. For example, the active matrix organic light-emitting diode (AM-OLED), in which each pixel is attached to a transistor and a capacitor, has a multiple-stack geometry with both planar and concave–convex architectures.<sup>21</sup> For the electrodes in AM-OLEDs to be replaced with CVD graphene, graphene must overcome its

<sup>a</sup>Department of Physics and SAINT, Sungkyunkwan University, Suwon 440-746, Republic of Korea. E-mail: jrahn@skku.edu

<sup>b</sup>Department of Physics, Kyonggi University, Suwon 443-760, Republic of Korea. E-mail: shju@kgu.ac.kr

<sup>c</sup>Pohang Accelerator Laboratory, Pohang University of Science and Technology, Pohang 790-784, Republic of Korea

<sup>d</sup>Interdisciplinary School of Green Energy, Ulsan National Institute of Science and Technology (UNIST), Ulsan 689-798, Republic of Korea

<sup>e</sup>School of Nano-Bioscience and Chemical Engineering, Ulsan National Institute of Science and Technology (UNIST), Ulsan 689-798, Republic of Korea.

E-mail: skkwak@unist.ac.kr

† Electronic supplementary information (ESI) available: Various concave–convex graphene–SiO<sub>2</sub> laminates, scanning electron microscopy images before and after the 3D lamination, influence of the size and gradient of the convex SiO<sub>2</sub> architecture on graphene lamination, spatial distributions of chemical configurations on graphene on the 3D laminate, and calculations of average strain (%). See DOI: 10.1039/c5nr04004c

‡ These authors have contributed equally to this work.

intrinsic preference for planar geometry. The development of real devices with complicated architecture thus requires CVD graphene to be adaptable to such architectures. Naturally, this requirement leads to the questions whether CVD graphene can be transferred onto complicated 3D architectures and how the physical properties of CVD graphene will change on such an architecture. Furthermore, 3D electrodes in various electronic devices with higher surface-to-volume ratios exhibit both improved efficiency and decreased current density, thereby enhancing the overall performance of the devices.<sup>20,22,23</sup> Therefore, research on the development of 3D materials in the form of graphene–insulator laminates is currently required.

Here, we demonstrate that 3D graphene–silicon dioxide (SiO<sub>2</sub>) laminates can be achieved in a controlled manner. CVD single-layer graphene grown on a copper foil was transferred onto SiO<sub>2</sub> samples of a concave–convex architecture in a seamless and uniform manner by thermal treatment, as observed by scanning electron microscopy (SEM). The seamless lamination was also successfully applied to indium thin oxide (ITO) that has been widely used in displays, resulting in a 3D graphene–ITO laminate. The geometry of the 3D graphene–SiO<sub>2</sub> laminates was successfully controlled by designing an appropriate SiO<sub>2</sub> architecture. When the amount of liquid poly(methyl methacrylate) (PMMA) on graphene transferred onto a 3D architecture was properly controlled by using spin coating, we were able to laminate even an extreme 3D architecture with both a negatively curved side and a great height. The strain in the convex graphene–SiO<sub>2</sub> laminates gradually varied from top to bottom, with a maximum strain at the edge of the top face, as observed by confocal Raman microscopy, and the 3D strained graphene–SiO<sub>2</sub> laminates were stable. The stability of the 3D laminates and their spatially resolved strain were systematically reproduced by molecular dynamics (MD) simulations based on a geometry similar to the convex graphene–SiO<sub>2</sub> architecture. Four-point probe measurements indicate that the electrical resistance of 3D graphene–SiO<sub>2</sub> laminates with heights less than 100 nm is similar to that of planar graphene–SiO<sub>2</sub> laminates. We further succeeded in controlling the electrical resistance of the 3D laminates by adjusting their heights. The achievement of 3D graphene–SiO<sub>2</sub> and graphene–ITO laminates in a controlled manner will accelerate the movement toward 3D graphene applications in real devices.

## Results and discussion

Fig. 1 shows representative images of 3D graphene–SiO<sub>2</sub> laminates. Various 3D SiO<sub>2</sub> architectures were produced by photolithography. Single-layer graphene grown on a copper foil by CVD was transferred onto the 3D SiO<sub>2</sub> architectures using PMMA (Fig. 1a and ESI, Fig. S1†). Subsequently, the graphene–SiO<sub>2</sub> architecture was thermally annealed at 130 °C to melt the PMMA before its removal.<sup>24</sup> Thermal annealing with the molten PMMA enabled the seamless and uniform lamination of graphene onto the 3D SiO<sub>2</sub> architecture,<sup>25–27</sup> as observed by SEM imaging. Both convex (Fig. 1b) and concave (Fig. 1c)

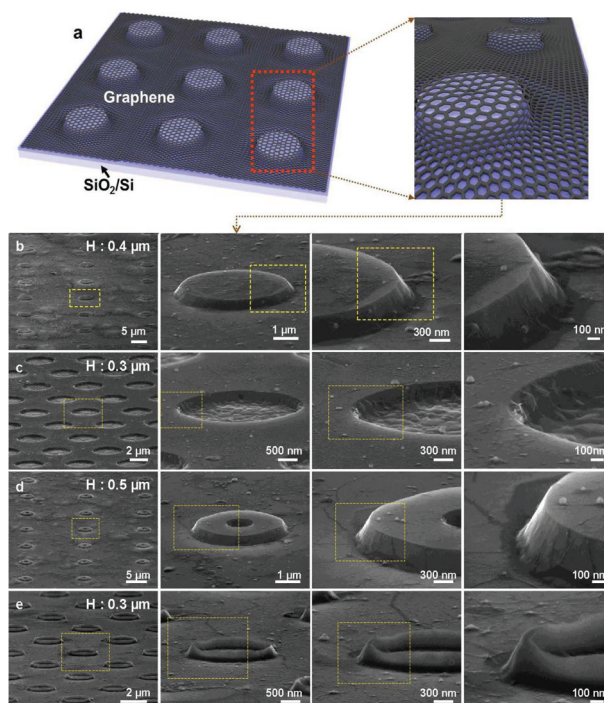


**Fig. 1** SEM images of various concave–convex graphene–SiO<sub>2</sub> laminates. (a) A schematic drawing of a 3D graphene–SiO<sub>2</sub> laminate that was produced by transferring CVD graphene to a convex SiO<sub>2</sub> architecture. (b–e) SEM images of various concave–convex graphene–SiO<sub>2</sub> laminates: convex (b), concave (c), and donut structures (d and e). The regions denoted by dashed rectangles are shown as magnified images. *H* is the height of the architecture.

architectures were successfully laminated with graphene. More complicated SiO<sub>2</sub> architectures, such as a doughnut (Fig. 1d, e and ESI, Fig. S1†), were also laminated with graphene. SEM images before and after the lamination were obtained so that the lamination was confirmed by comparing the SEM images (ESI, Fig. S2†). The small features on the 3D graphene–SiO<sub>2</sub> laminates are small particles laminated with graphene, where the small particles can be produced during the patterning process of the SiO<sub>2</sub> architectures or during the transfer of graphene. The small features thus do not indicate that graphene is floating on the Si architecture. There were studies on the adhesion of CVD graphene onto nanostructures. The formation of wrinkling and delamination of CVD graphene were observed on convex structures such as nanoparticles<sup>28</sup> or nanopillars.<sup>29,30</sup> The mechanisms of the wrinkling and delamination were the focus of the studies. On the concave structures,<sup>31,32</sup> floating graphene formed and the structure of the floating graphene was controlled. In this study, both convex and concave structures were laminated with CVD graphene without delamination and formation of floating graphene. The influence of the size and gradient of the SiO<sub>2</sub> architecture on the lamination was further studied. Lamination was still achieved even when the size of the convex SiO<sub>2</sub> architecture was increased (ESI, Fig. S3a and b†). However,

when the angle of inclination was greater than  $90^\circ$ , graphene did not attach to the side of the convex  $\text{SiO}_2$  architecture but floated instead (ESI, Fig. S3c and d<sup>†</sup>), which was confirmed by comparing SEM images before and after the lamination (ESI, Fig. S4<sup>†</sup>).

To understand the origin of the geometrical limit of the 3D lamination, an extreme 3D architecture with both a negatively curved side and a great height was fabricated by using ITO that has been widely used in displays (Fig. 2). The height of the pillar-like ITO structure is  $5\ \mu\text{m}$  and the side near the edge of the top has an angle of inclination above  $90^\circ$ . When the same lamination process as the  $\text{SiO}_2$  architecture was applied to the ITO architecture (Fig. 2a–d), the graphene was floating on the ITO architecture even after it was annealed at a high temperature. This result suggests that there is an important parameter in the lamination of a 3D architecture that is different from the lamination of a planar structure. After manipulating various parameters of the 3D lamination, it was found that a thick liquid PMMA film must be spin-coated after graphene is transferred onto a 3D architecture (Fig. 2e–h). When the amount of spin-coated liquid PMMA film exceeded a critical value, the overall structure of the extreme 3D ITO architecture was laminated with graphene (Fig. 2e and i). After annealing at  $130\ ^\circ\text{C}$ , the 3D lamination was completed (Fig. 2f and j). The thicknesses of the PMMA films that were coated during the lamination process were measured using cross-sectional SEM images (ESI, Fig. S5<sup>†</sup>). The results suggest that the thick liquid PMMA during the spin coating contributes to the bending of graphene and the attachment of bent graphene

to a 3D architecture. It was also successfully achieved to laminate an extreme 3D architecture with both a negative curvature and a great height by controlling the spin coating of a liquid PMMA film. The achievement of the lamination of the extreme 3D architecture with graphene suggests the origin of the seamless lamination. The essential requirement for the lamination is external pressure to stretch graphene. The external pressure in this system can be induced by not only the weight of liquid PMMA but also the spinning during the spin coating of liquid PMMA.

To understand the spatial variation of the intrinsic structure of the curved graphene laminated onto the 3D  $\text{SiO}_2$  architecture, confocal Raman spectroscopy experiments were performed with a spatial resolution of  $500\ \text{nm}$ . Fig. 3 shows representative Raman spectra of graphene on a convex  $\text{SiO}_2$  architecture with a truncated cone shape, a height of  $490\ \text{nm}$ , top and base radii of  $4$  and  $5.5\ \mu\text{m}$ , respectively, and an angle of inclination of  $20^\circ$ . The D, G, and 2D peaks, which are the typical features of the Raman spectra of graphene, originate from the TO phonon at the K point of the Brillouin zone (BZ) of graphene, the breathing modes of  $\text{sp}^2$  carbon atoms, and two phonons with opposing momentum in the highest optical branch near the K point, respectively.<sup>33–37</sup> The D, G, and 2D Raman scattering peaks of pristine single-layer graphene occur at approximately  $1350$ ,  $1580$ , and  $2690\ \text{cm}^{-1}$ , respectively.<sup>38</sup> Spatially resolved Raman spectra were recorded from the center of the top face to the bottom (Fig. 3a and b). The blue shifts of the G and 2D peaks at the bottom (E point in Fig. 3a) compared to those of the pristine graphene can be ascribed to

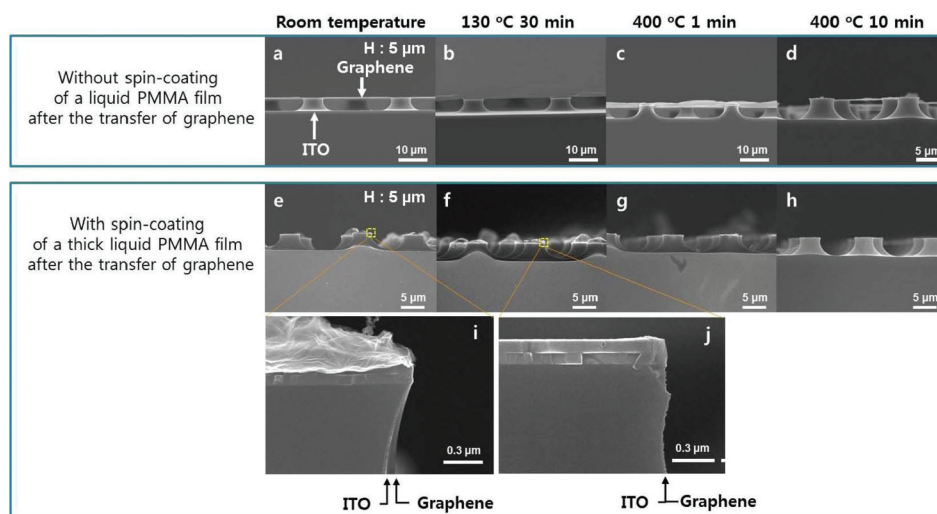


**Fig. 2** SEM images of graphene–ITO laminates. (a–d) SEM images of graphene that is floating on a 3D ITO architecture, which were observed when a spin-coated liquid PMMA film was not used after the transfer of graphene onto the 3D architecture. In (a), the SEM image was acquired after the transfer of graphene on the 3D architecture. In (b)–(d), the SEM images were acquired after subsequent annealing at  $130\ ^\circ\text{C}$  for 30 minutes (b),  $400\ ^\circ\text{C}$  for 1 minute (c), and  $400\ ^\circ\text{C}$  for 10 minutes (d), respectively. (e–h) SEM images of a 3D graphene–ITO laminate that were observed when a spin-coated liquid PMMA film was used after the transfer of graphene onto the 3D architecture. In (e), the SEM image was acquired after a thick liquid PMMA film was spin-coated on graphene transferred onto the 3D architecture. In (f)–(h), the SEM images were acquired after subsequent annealing at  $130\ ^\circ\text{C}$  for 30 minutes (f),  $400\ ^\circ\text{C}$  for 1 minute (g), and  $400\ ^\circ\text{C}$  for 10 minutes (h), respectively. (i and j) Enlarged SEM images of the regions denoted by rectangles in (e) and (f), respectively.  $H$  is the height of the architecture.

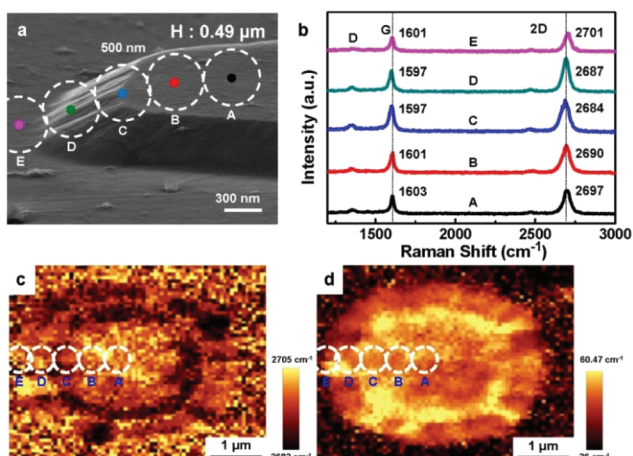


**Fig. 3** Confocal Raman spectra and maps of the convex  $\text{SiO}_2$ -graphene laminates. (a) SEM image of the convex graphene- $\text{SiO}_2$  laminate with a truncated cone shape, where the dashed circles denote the spatial resolution of the Raman spectra. (b) Raman spectra recorded at the positions marked in (a). (c-d) Raman spectral maps of the position (c) and FWHM (d) of the 2D peak.  $H$  is the height of the architecture.

a hole-doping effect caused by the  $\text{SiO}_2$  substrate or the surrounding environment during the thermal annealing step that was performed in the sample preparation stage to enable stronger adhesion between the graphene and the substrate, as observed on planar graphene- $\text{SiO}_2$  laminates.<sup>39,40</sup> Compared to the bottom and the center of the top face (A point in Fig. 3a), a red shift was observed for both the G and 2D peaks at the inclined plane (D point), the edge (C point), and the off-center position (B point) of the top face. There exist three representative types of strain: uniaxial, biaxial, and shear strain.<sup>41,42</sup>

To understand which type of strain is similar to the strain on the truncated cone, we performed MD simulations, based on a force field that properly handles the bonding and non-bonding interactions of atoms (Fig. 4). Single-layer

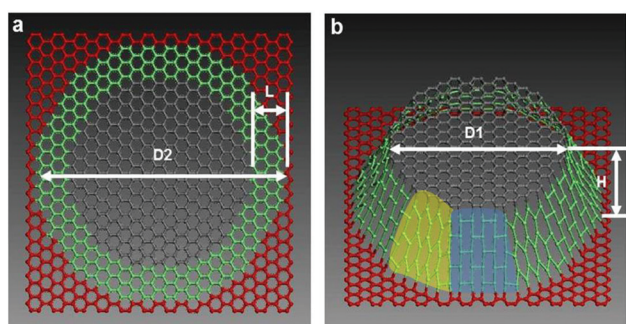


**Fig. 4** MD simulations for the strain on the 3D truncated cone. (a) Model geometry of a graphene sheet, where the carbon atoms in the red region outside the truncated cone shape of diameter  $D_2$  were fixed. (b) A convex pattern deformed by the pressing force with a diameter of  $D_1$ . Only the carbon atoms in the green-colored region were relaxed, where  $L$  is the width of the green-colored region and the atoms in the gray-colored region were fixed at a height of  $H$ .

graphene, shaped in the form of a truncated cone, was used without a substrate (Fig. 4). This simulation focused on the strain effect on the inclined plane of the truncated cone-shaped graphene. Thus, during the formation of the truncated cone-shaped graphene (Fig. 4b) using square-shaped graphene (Fig. 4a), only the carbon atoms of the inclined plane were relaxed, with fixation of the carbon atoms on the top or bottom face. Because the Raman experiments suggest that graphene on the top is nearly unstrained and geometrically isotropic, the simplified model can reflect qualitatively the experimental system. MD simulations of fully-relaxed truncated cone shaped graphene on a  $\text{SiO}_2$  substrate are described in Fig. 5. As shown in Fig. 4, the carbon atoms inside the inner circle with a diameter of  $D_1$  were raised along the vertical direction by a height of  $H$  (Fig. 4b), and the carbon atoms outside the outer circle with a diameter of  $D_2$  (Fig. 4a) were fixed. The MD simulations suggest that the strain on the

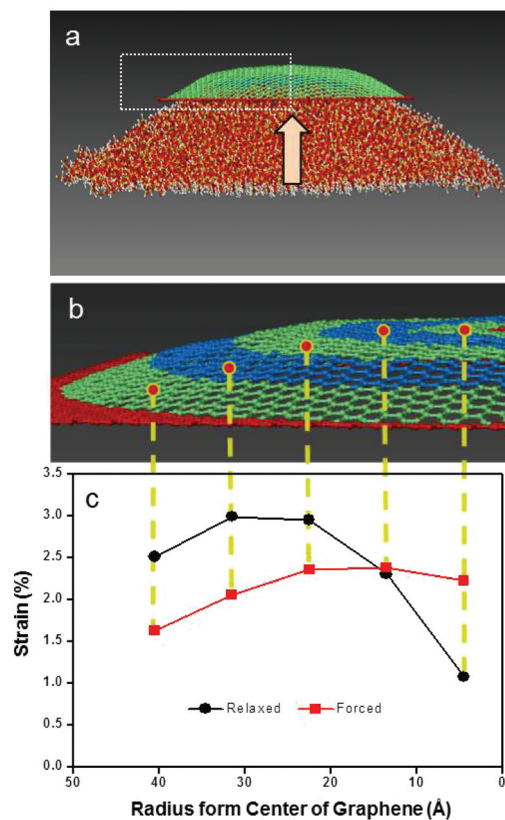


**Fig. 5** MD simulations for studying the spatially varying strain on the convex graphene- $\text{SiO}_2$  laminates. (a) Graphene was strained by the  $\text{SiO}_2$  substrate. The yellow arrow indicates the pressing direction. (b) The strained graphene in (a) shown without the  $\text{SiO}_2$  substrate. The colored stripes are used for clarity in the identification of different regions. (c) Plot of strain as a function of the distance from the center of the graphene. The filled red squares represent the strain (i.e.,  $|(a - a_0)/a_0| \times 100\%$  where  $a$  and  $a_0$  are the average bond lengths of strained and unstrained graphene, respectively) in the strained graphene pushed by the  $\text{SiO}_2$  substrate, and the filled black circles represent those in the strained and relaxed graphene pushed by the  $\text{SiO}_2$  substrate.

3D truncated cone is closer to biaxial strain rather than uniaxial strain, as reported in Raman experiments.<sup>42,43</sup>

For graphene under biaxial strain, the following phenomena could occur: softening (red shift) of the G and 2D peaks due to tensile strain and the shift of the 2D peak is greater than that of the G peak.<sup>35,42,43</sup> The red shifts and broadening of the G and 2D peaks at positions between the bottom and the center of the top face can thus be assigned to the strain effect in graphene. The red shift of the 2D peak suggests that the strain has a maximum value at the edge of the top face. For the biaxial strain, the reported shifts of the 2D peak, which was induced by strain (%), is  $140 \text{ cm}^{-1}/\%$ , where the strain (%) is  $|(a - a_0)/a_0| \times 100\%$  and  $a$  and  $a_0$  are the average lattice constant of the strained graphene and the lattice constant of pristine graphene, respectively.<sup>35,41</sup> The strains (%), compared to the bottom (E point), at the inclined plane (D point), the edge of the top face (C point), the off-center position of the top face (B point), and the center (A point) of the top face are thus approximately 0.1, 0.12, 0.08, and 0.03%, respectively, based on the reported shifts of the 2D peak. The strain effect is more clearly illustrated by the Raman maps of the position (Fig. 3c) and the FWHM (Fig. 3d) of the 2D peak; the darker region (larger red shift) in the position mapping is brighter (enhanced broadening) in the FWHM mapping. Details of the strain effect on the 3D graphene–SiO<sub>2</sub> laminates based on MD simulations will be discussed later. On the other hand, a lack of hole doping at the edge (C point) can explain the spatial variation of the position of the 2D peak, where hole doping results in a blue shift of the 2D peak.<sup>40</sup> In this case, the FWHM of the 2D peak at the edge (C point) should be narrower than those at the center of the top face (A point) and the bottom (E point) because hole doping broadens the FWHM of the 2D peak.<sup>42</sup> However, the FWHM of the 2D peak at the edge (C point) is wider than those at the center of the top face (A point) and the bottom (E point). Therefore, the hole doping cannot be the origin of the spatial variation of the 2D peak. On the other hand, chemical reactions between PMMA and graphene, when annealed at high temperatures, can shift the 2D peak. The chemical reactions were reported to shift the 2D peak to the higher frequency side, resulting in a blue shift.<sup>44</sup> Therefore, the chemical reactions at high temperatures cannot explain the red shift of the 2D peak of the graphene on the 3D laminates and can be excluded from the origin of the shift of the 2D peak. Furthermore, spatial distributions of chemical configurations of the graphene on the 3D laminates were studied using scanning photoemission microscopy (SPEM) with synchrotron radiation (ESI, Fig. S6†). SPEM experiments were performed at the 8A1 beamline, Pohang Light Source (PLS). C 1s spectra were recorded using a photon energy of 630 eV and its spatial resolution was 300 nm. Fig. S5a† shows the schematic drawing of the SPEM experiment. A zone plate was used to focus an X-ray beam close to the sample so that a detector was located at a grazing angle. The shape of the graphene on the 3D laminate was confirmed by measuring the spatial distribution of photoelectron intensity with a binding energy window between 280 and 292 eV (ESI, Fig. S6b†). Here,

because the focal point was fixed at the top of the 3D laminate during the scanning, a brighter image can be obtained at the top with respect to the bottom. The darker region, which is located at the opposite side of the detector, is obtained because photoelectrons are partially screened by the 3D structure. After determining the shape of the 3D laminate, spatially-resolved C 1s spectra were recorded (ESI, Fig. S6c and d†). As shown in Fig. S6c and d,† the C 1s spectra were identical, where the spectra were recorded at the top, inclined slope, and bottom, as indicated by the number in Fig. S6b.†<sup>45,46</sup> The C 1s spectra are overlapped in Fig. S6c† and spread out in Fig. S6d.† The identical C 1s spectra suggest that the chemical configurations of graphene are very uniform on the 3D laminate although fragments of PMMA can exist on the graphene after the heating treatment. The SPEM experiments support that the Raman shift is induced by strain rather than different chemical distributions.

To obtain a systematic understanding of the strain of graphene on the 3D SiO<sub>2</sub> architecture, MD simulations were further performed (Fig. 5). The spatially varying strain of graphene on the convex SiO<sub>2</sub> structure was studied, where the strain was estimated by the C–C bond distribution (Fig. 5). An amorphous SiO<sub>2</sub> structure with a truncated cone shape was constructed to act as a substrate. Only the circular area of the square-shaped graphene was relaxed to be strained by the SiO<sub>2</sub> pressing, and when the vertical motion of the pressing reaches a distance consistent with the aspect ratio of the pressing ( $H/L \sim 0.33$ ), all of the carbon atoms in the graphene are relaxed to enable some of the carbon atoms to adhere to the surface of SiO<sub>2</sub> (Fig. 5a). The colored stripes in the adhered shape of graphene (Fig. 5b) represent each section for the strain calculation, which correspond to the points in the plot (Fig. 5c) of strain against the radius of the originally circular area of graphene. Here, the strain used in the simulations is the change in the average of all bonds contained in each stripe, as defined in the Raman spectral analysis. The plot in Fig. 5c shows how the strain evolved from the fixed graphene to the relaxed graphene along the radial direction. The central region of the fixed graphene changes from the most strained to the most relaxed region by freeing the constrained carbon atoms during the simulation. Here, the basis length of the bond for the strain calculation is extracted from the average bond length in the central region, which was estimated to be approximately 1.37 Å. As shown in Fig. 5c, the strain toward the circular center is very small. In contrast, we found the largest strain at the inclined plane in the vicinity of the edge and the smallest strain towards the bottom. As observed from the confocal Raman spectra (Fig. 3b), the strain of the graphene on the convex SiO<sub>2</sub> architecture was also maximized at the inclined plane in the vicinity of the edge and minimized at the circular center. Thus, the spatially varying strain observed in the simulations qualitatively follows the experimental observation. On the other hand, there is a discrepancy in quantitative values of the strain. The discrepancy is mainly because of the limited size of graphene in the simulations. In the experiments, the strain on the 3D architecture can be further relaxed

through graphene at the bottom that is located between the 3D architectures. In comparison to the experiments, graphene at the bottom in the simulations (Fig. 5b), which is denoted by red spheres, needs to be fixed in the geometry. For the structure that was used in the simulations, when graphene at the bottom is fixed (ESI, Fig. S7a<sup>†</sup>), the average strain is 2.33%, which is consistent with the MD simulations. When graphene at the bottom is relaxed (ESI, Fig. S7b<sup>†</sup>), the average strain is reduced to 0.77%, for example. Therefore, the discrepancy in quantitative values of the strain means that graphene at the bottom during the experimental lamination also contributes to the strain relaxation of graphene on a 3D architecture.

The changes in the strain of graphene on a convex SiO<sub>2</sub> architecture on increasing the height of the convex architecture were further studied. Raman spectra were recorded from graphene on the truncated cone-shaped architectures with different heights. The position of the 2D peak in Fig. 6 is an average value of those that were measured from different truncated cone-shaped architectures with the same height. The height was changed from 100 nm to 1 μm. As shown in Fig. 6, both the positions of the 2D peaks of the top face and the inclined plane gradually shifted toward the red side on increasing the height. The shifts of the 2D peaks suggest that the strain of graphene on the truncated cone-shaped architecture is enhanced on increasing the height and can be controlled by its geometry.

The variation in the sheet resistance of the 3D graphene–SiO<sub>2</sub> laminates, compared to that of planar graphene–SiO<sub>2</sub> laminates, was measured to understand the influence of the strain on electrical transport using four-point probe measurements (Fig. 7a–c). The same CVD graphene was transferred onto both the planar (lower channel) and 3D (upper channel) SiO<sub>2</sub> substrates to exclude variations in resistance due to the quality of the graphene; for these substrates, the width and length of the channel were 10 and 100 μm, respectively, and ten convex structures with a width of 5 μm were periodically arrayed with a separation of 5 μm in the upper channel. The array of the convex structure can correspond to an alternating 1D array of convex and concave structures because the width is equal to the separation. The average sheet resistance of the planar graphene–SiO<sub>2</sub> laminates was 2.0 kΩ □<sup>-1</sup> (Fig. 7d). When the height of the convex graphene–SiO<sub>2</sub> structure was 100 nm, the sheet resistance did not differ significantly from that of the planar structure. When the height was increased to 300 nm while maintaining the width of the convex structure, the average sheet resistance increased to 16.4 kΩ □<sup>-1</sup>. The average sheet resistance became approximately 100 kΩ □<sup>-1</sup> when the height reached 1 μm. The relationship between the sheet resistance and the height of the convex structure suggests that the sheet resistance of the 3D graphene–SiO<sub>2</sub> architecture can be controlled by using its geometry. The variation in the sheet resistance is similar to the change in strain, which is determined from the shift of the 2D peak in a Raman spectrum (Fig. 6). The variation in the sheet resistance can thus be explained in terms of the strained graphene. Such an increase in the sheet resistance due to strain has been

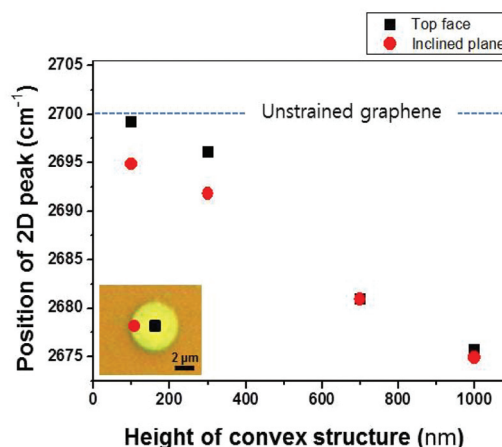


Fig. 6 Position of a 2D peak in a Raman spectrum of graphene as a function of the height of a truncated cone-shaped convex structure. The positions of the 2D peaks at the top face and the inclined plane are denoted by black solid rectangles and red solid circles, respectively. The inset is the representative optical image of the truncated cone-shaped convex structure.

observed on the stretched graphene.<sup>3</sup> The atomic structure of the stretched graphene results in the deformation of its electronic structure, thereby reducing the electron mobility along the direction of stretching.<sup>47</sup>

## Experimental

### Photolithography

Various concave–convex SiO<sub>2</sub> patterns were generated by a conventional photolithography process. The entire area was coated with a photoresist and covered with a photomask designed with various concave–convex patterns. Subsequently, the area was illuminated with ultraviolet light to remove the photoresist in a selective manner. After removing the SiO<sub>2</sub> layer that was not covered with the photoresist by a buffered oxide etchant, the remaining photoresist was removed to reveal a concave–convex pattern made from the SiO<sub>2</sub> layer.

### Fabrication of 3D graphene–SiO<sub>2</sub> laminates

For the growth of single-layer graphene, a Cu foil with a thickness of 25 μm (Alfa Aesar) was placed at the center of a quartz tube and was annealed for two hours at 1000 °C with a H<sub>2</sub> gas flow of 100 sccm. Subsequently, the Cu foil was further annealed for 30 minutes with a CH<sub>4</sub> gas flow of 20 sccm and a H<sub>2</sub> gas flow of 100 sccm at the same temperature. After rapidly cooling to room temperature, the graphene grown on Cu foil was coated with PMMA. The Cu foil was removed by using an etchant (CE-100, Transene Company) and washed with distilled (DI) water. The sample was then immersed in HNO<sub>3</sub> for 10 minutes and subsequently washed with DI water to remove the remaining Cu residues. The resulting PMMA/graphene sheet was transferred onto a SiO<sub>2</sub> substrate with a concave–

convex structure and was subsequently dried in an oven at 50 °C for 30 minutes. To achieve a stronger adhesion between the graphene and the concave–convex SiO<sub>2</sub> architecture, the samples were further dried on a hot plate at 130 °C, which is close to the melting point of PMMA, for two hours. Finally, the PMMA was removed using acetone and chloroform.

### Confocal Raman spectroscopy

A frequency-doubled Nd:YAG laser with a wavelength of 532 nm and an average power of 1 mW was used for Raman analysis (CRM200, Witec).

### Four-point probe measurements

The variation in the sheet resistance of the 3D graphene–SiO<sub>2</sub> laminates, compared to those of planar graphene–SiO<sub>2</sub> laminates, was measured to understand the influence of the strain on electrical transport using four-point probe measurements (Fig. 7a–c). Two probes (A and D probes) carry the current and the other two probes (B and C probes) sense the voltage. By measuring the voltage drop, the sheet resistance of graphene was calculated. The sheet resistance of graphene was measured using a semiconductor device parameter analyzer (Agilent, B1500A) at room temperature under ambient air.

### Molecular dynamics simulation

As shown in Fig. 4, two square-shaped, single-layer graphene structures with dimensions of 5.3 nm × 5.3 nm and 10 nm × 9.8 nm were modeled with carbon atoms, the lengths of which were adjusted to be approximately 1.42 nm. Each single-layer graphene structure was placed in the *x*–*y* plane in different simulation boxes with sizes of 7.9 nm × 7.9 nm × 7.9 nm and 16 nm × 16 nm × 12 nm, which were sufficiently large to

accommodate vertically stretched graphene sheets. After modeling the relaxation of the carbon atoms with an all-atom MD simulation at 298 K for 1 picosecond (ps), the simulation was switched to run the MD with a micro-canonical (constant energy) ensemble at a time step of 1 femtosecond (fs). The force was implemented by creating an invisible object that is 105 times heavier than the carbon atoms under the press and by pushing with a velocity of 100 Å ps<sup>-1</sup>. A force from the circular press was applied in the vertical direction on the gray area (Fig. 4b) in the single-layer graphene, while the carbon atoms in the colored circular shell (Fig. 4a) were set to be stretchable. Bond and non-bond interactions were calculated by the COMPASS force field,<sup>48</sup> which treats constituent carbons as sp<sup>2</sup> hybridized carbon without applying electrostatic forces. As shown in Fig. 5, a single-layer graphene structure with dimensions of 10 nm × 9.8 nm is placed above a truncated cone-shaped SiO<sub>2</sub>, which is amorphously constructed with an aspect ratio of 0.333. The SiO<sub>2</sub> substrate, which is hydrogenated, contains 27 954 atoms. To decrease the simulation time, we performed a micro-canonical straining simulation, which pushes the graphene from the bottom of the substrate until the bond length reaches ~1.5 nm at room temperature. The percentage strains of the final simulation configuration were calculated and are plotted in Fig. 5c ('forced'). In this particular simulation, because the outer region of the graphene is fixed in space, the estimated strains are not the true strains. To obtain an appropriate strain distribution, the fixed graphene region was released and simulated at the experimental temperature of 403 K. The MD with a canonical ensemble (constant temperature) was run with a time step of 0.01 fs for 2 ps. During the simulation, all the bond lengths were monitored, and their variations are plotted in Fig. 5c ('relaxed') for the same force field described above.

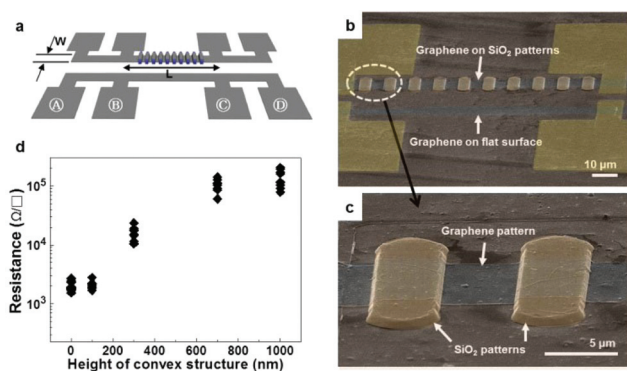


**Fig. 7** Four-point probe measurements of the sheet resistivity of the convex SiO<sub>2</sub>–graphene laminates. (a) Schematic diagram of the pattern used for the sheet resistance measurement, where resistivity was measured by using the D-electrode pad as a ground, applying a constant current to the A-electrode pad, and measuring the voltage drop between the B-electrode pad and the C-electrode pad. (b–c) SEM images of the convex (upper channel) and planar (lower channel) graphene–SiO<sub>2</sub> laminates, where the graphene patterns are highlighted in blue. (d) Sheet resistance of the graphene–SiO<sub>2</sub> laminates as a function of the height of the convex structure.

## Conclusions

3D graphene–SiO<sub>2</sub> laminates were successfully fabricated using various SiO<sub>2</sub> concave–convex architectures. We found that there are geometrical limitations in achieving uniform and seamless lamination. The geometrical limitations were overcome by enhancing the pressure applied to graphene that is induced by not only the weight of liquid PMMA but also spinning during the spin coating of liquid PMMA, resulting in the first successful lamination of extreme 3D architectures with graphene. The graphene on the convex SiO<sub>2</sub> architecture was strained, with a maximum value near the edge of the top face, and the strain was reduced at the inclined plane compared to that on the top face; these observations of the strain were systematically reproduced by using MD simulations. The sheet resistance of the graphene on the convex architecture, which is related to the strain of the graphene, was further controlled by using its geometry. These results will systematically guide research on the applications of CVD graphene to complicated, real 3D electronic devices, where the electric properties

of graphene on the 3D laminates can be predicted using MD simulations, based on our systematic study.

## Acknowledgements

This study was supported by a grant from the National Research Foundation of Korea (NRF-2015R1A2A2A01004853). SJ was supported by a National Research Foundation of Korea (NRF) grant funded by the Korean government (MSIP) (2014R1A2A1A11049450 and 2015M2B2A9028357).

## Notes and references

- 1 K. S. Novoselov, A. K. Geim, S. V. Morozov, D. Jiang, M. I. Katsnelson, I. V. Grigorieva, S. V. Dubonos and A. A. Firsov, *Nature*, 2005, **438**, 197–200.
- 2 Y. B. Zhang, Y. W. Tan, H. L. Stormer and P. Kim, *Nature*, 2005, **438**, 201–204.
- 3 K. S. Kim, Y. Zhao, H. Jang, S. Y. Lee, J. M. Kim, K. S. Kim, J. H. Ahn, P. Kim, J. Y. Choi and B. H. Hong, *Nature*, 2009, **457**, 706–710.
- 4 B. J. Kim, H. Jang, S. K. Lee, B. H. Hong, J. H. Ahn and J. H. Cho, *Nano Lett.*, 2010, **10**, 3464–3466.
- 5 M. Choucair, P. Thordarson and J. A. Stride, *Nat. Nanotechnol.*, 2009, **4**, 30–33.
- 6 X. S. Li, W. W. Cai, J. H. An, S. Kim, J. Nah, D. X. Yang, R. Piner, A. Velamakanni, I. Jung, E. Tutuc, S. K. Banerjee, L. Colombo and R. S. Ruoff, *Science*, 2009, **324**, 1312–1314.
- 7 Y. M. Lin, C. Dimitrakopoulos, K. A. Jenkins, D. B. Farmer, H. Y. Chiu, A. Grill and P. Avouris, *Science*, 2010, **327**, 662–662.
- 8 Y. Q. Wu, Y. M. Lin, A. A. Bol, K. A. Jenkins, F. N. Xia, D. B. Farmer, Y. Zhu and P. Avouris, *Nature*, 2011, **472**, 74–78.
- 9 X. C. Miao, S. Tongay, M. K. Petterson, K. Berke, A. G. Rinzler, B. R. Appleton and A. F. Hebard, *Nano Lett.*, 2012, **12**, 2745–2750.
- 10 R. H. Kim, M. H. Bae, D. G. Kim, H. Y. Cheng, B. H. Kim, D. H. Kim, M. Li, J. Wu, F. Du, H. S. Kim, S. Kim, D. Estrada, S. W. Hong, Y. G. Huang, E. Pop and J. A. Rogers, *Nano Lett.*, 2011, **11**, 3881–3886.
- 11 S. Bae, H. Kim, Y. Lee, X. F. Xu, J. S. Park, Y. Zheng, J. Balakrishnan, T. Lei, H. R. Kim, Y. I. Song, Y. J. Kim, K. S. Kim, B. Ozyilmaz, J. H. Ahn, B. H. Hong and S. Iijima, *Nat. Nanotechnol.*, 2010, **5**, 574–578.
- 12 Z. H. Sun, Z. K. Liu, J. H. Li, G. A. Tai, S. P. Lau and F. Yan, *Adv. Mater.*, 2012, **24**, 5878–5883.
- 13 J. Yao, J. Lin, Y. H. Dai, G. D. Ruan, Z. Yan, L. Li, L. Zhong, D. Natelson and J. M. Tour, *Nat. Commun.*, 2012, **3**, 1101.
- 14 A. N. Sidorov, A. Sherehiy, R. Jayasinghe, R. Stallard, D. K. Benjamin, Q. K. Yu, Z. H. Liu, W. Wu, H. L. Cao, Y. P. Chen, Z. G. Jiang and G. U. Sumanasekera, *Appl. Phys. Lett.*, 2011, **99**, 013115.
- 15 T. Georgiou, R. Jalil, B. D. Belle, L. Britnell, R. V. Gorbachev, S. V. Morozov, Y. J. Kim, A. Gholinia, S. J. Haigh, O. Makarovskiy, L. Eaves, L. A. Ponomarenko, A. K. Geim, K. S. Novoselov and A. Mishchenko, *Nat. Nanotechnol.*, 2013, **8**, 100–103.
- 16 H. C. Shin, Y. Jang, T. H. Kim, J. H. Lee, D. H. Oh, S. J. Ahn, J. H. Lee, Y. Moon, J. H. Park, S. J. Yoo, C. Y. Park, D. Whang, C. W. Yang and J. R. Ahn, *J. Am. Chem. Soc.*, 2015, **137**, 6897–6905.
- 17 Z. P. Chen, W. C. Ren, L. B. Gao, B. L. Liu, S. F. Pei and H. M. Cheng, *Nat. Mater.*, 2011, **10**, 424–428.
- 18 J. H. Park, D. H. Cho, Y. Moon, H. C. Shin, S. J. Ahn, S. K. Kwak, H. J. Shin, C. Lee and J. R. Ahn, *ACS Nano*, 2014, **8**, 11657–11665.
- 19 J. S. Lee, *J. Mater. Chem.*, 2011, **21**, 14097–14112.
- 20 J. Heikenfeld, K. Zhou, E. Kreit, B. Raj, S. Yang, B. Sun, A. Milarcik, L. Clapp and R. Schwartz, *Nat. Photonics*, 2009, **3**, 292–296.
- 21 B. Geffroy, P. Le Roy and C. Prat, *Polym. Int.*, 2006, **55**, 572–582.
- 22 D. E. Johnston, K. G. Yager, C. Y. Nam, B. M. Ocko and C. T. Black, *Nano Lett.*, 2012, **12**, 4181–4186.
- 23 B. Z. Tian, T. Cohen-Karni, Q. Qing, X. J. Duan, P. Xie and C. M. Lieber, *Science*, 2010, **329**, 830–834.
- 24 D. J. Plazek, *Rheol. Acta*, 1974, **13**, 367–376.
- 25 X. S. Li, Y. W. Zhu, W. W. Cai, M. Borysiak, B. Y. Han, D. Chen, R. D. Piner, L. Colombo and R. S. Ruoff, *Nano Lett.*, 2009, **9**, 4359–4363.
- 26 X. L. Liang, B. A. Sperling, I. Calizo, G. J. Cheng, C. A. Hacker, Q. Zhang, Y. Obeng, K. Yan, H. L. Peng, Q. L. Li, X. X. Zhu, H. Yuan, A. R. H. Walker, Z. F. Liu, L. M. Peng and C. A. Richter, *ACS Nano*, 2011, **5**, 9144–9153.
- 27 Z. G. Cheng, Q. Y. Zhou, C. X. Wang, Q. A. Li, C. Wang and Y. Fang, *Nano Lett.*, 2011, **11**, 767–771.
- 28 M. Yamamoto, O. Pierre-Louis, J. Huang, M. S. Fuhrer, T. L. Einstein and W. G. Cullen, *Phys. Rev. X*, 2012, **2**, 041018.
- 29 H. Tomori, A. Kanda, H. Goto, Y. Ootuka, K. Tsukagoshi, S. Moriyama, E. Watanabe and D. Tsuya, *Appl. Phys. Express*, 2011, **4**, 075102.
- 30 G. X. Li, C. Yilmaz, X. H. An, S. Somu, S. Kar, Y. J. Jung, A. Busnaina and K. T. Wan, *J. Appl. Phys.*, 2013, **113**, 244303.
- 31 S. P. Koenig, N. G. Boddeti, M. L. Dunn and J. S. Bunch, *Nat. Nanotechnol.*, 2011, **6**, 543–546.
- 32 X. H. Liu, N. G. Boddeti, M. R. Szpunar, L. D. Wang, M. A. Rodriguez, R. Long, J. L. Xiao, M. L. Dunn and J. S. Bunch, *Nano Lett.*, 2013, **13**, 2309–2313.
- 33 A. C. Ferrari, *Solid State Commun.*, 2007, **143**, 47–57.
- 34 L. M. Malard, M. A. Pimenta, G. Dresselhaus and M. S. Dresselhaus, *Phys. Rep.*, 2009, **473**, 51–87.
- 35 T. M. G. Mohiuddin, A. Lombardo, R. R. Nair, A. Bonetti, G. Savini, R. Jalil, N. Bonini, D. M. Basko, C. Galiotis, N. Marzari, K. S. Novoselov, A. K. Geim and A. C. Ferrari, *Phys. Rev. B: Condens. Matter Mater. Phys.*, 2009, **79**, 205433.

- 36 A. Das, B. Chakraborty and A. K. Sood, *Bull. Mater. Sci.*, 2008, **31**, 579–584.
- 37 A. C. Ferrari, J. C. Meyer, V. Scardaci, C. Casiraghi, M. Lazzeri, F. Mauri, S. Piscanec, D. Jiang, K. S. Novoselov, S. Roth and A. K. Geim, *Phys. Rev. Lett.*, 2006, **97**, 187401.
- 38 P. Poncharal, A. Ayari, T. Michel and J. L. Sauvajol, *Phys. Rev. B: Condens. Matter Mater. Phys.*, 2008, **78**, 113407.
- 39 S. Ryu, L. Liu, S. Berciaud, Y. J. Yu, H. T. Liu, P. Kim, G. W. Flynn and L. E. Brus, *Nano Lett.*, 2010, **10**, 4944–4951.
- 40 A. Pirkle, J. Chan, A. Venugopal, D. Hinojos, C. W. Magnuson, S. McDonnell, L. Colombo, E. M. Vogel, R. S. Ruoff and R. M. Wallace, *Appl. Phys. Lett.*, 2011, **99**, 122108.
- 41 Z. H. Ni, T. Yu, Y. H. Lu, Y. Y. Wang, Y. P. Feng and Z. X. Shen, *ACS Nano*, 2008, **2**, 2301–2305.
- 42 J. Zabel, R. R. Nair, A. Ott, T. Georgiou, A. K. Geim, K. S. Novoselov and C. Casiraghi, *Nano Lett.*, 2012, **12**, 617–621.
- 43 C. Metzger, S. Remi, M. K. Liu, S. V. Kusminskiy, A. H. C. Neto, A. K. Swan and B. B. Goldberg, *Nano Lett.*, 2010, **10**, 6–10.
- 44 L. M. Malard, R. L. Moreira, D. C. Elias, F. Plentz, E. S. Alves and M. A. Pimenta, *J. Phys.: Condens. Matter*, 2010, **22**, 334202.
- 45 J. H. Park, W. Jung, D. Cho, J. T. Seo, Y. Moon, S. H. Woo, C. Lee, C. Y. Park and J. R. Ahn, *Appl. Phys. Lett.*, 2013, **103**, 171609.
- 46 Y. C. Lin, C. C. Lu, C. H. Yeh, C. H. Jin, K. Suenaga and P. W. Chiu, *Nano Lett.*, 2012, **12**, 414–419.
- 47 S. M. Choi, S. H. Jhi and Y. W. Son, *Phys. Rev. B: Condens. Matter Mater. Phys.*, 2010, **81**, 081407(R).
- 48 H. Sun, *J. Phys. Chem. B*, 1998, **102**, 7338–7364.